Research Article | Vol. 32, No. 14 / 1 Jul 2024 / Optics Express 23932
Optics EXPRESS

# Dependence of the Raman vibration modes on structural properties of Tm:$(Sc_xY_{1-x})_2O_3$ laser ceramics with $0 \leq x < 1$

Angela Pirri,[1,*] Alberto Santonocito,[2] Roman N. Maksimov,[3,4] Vladislav A. Shitov,[3] Maurizio Becucci,[5] Barbara Patrizi,[6] Matteo Vannini,[6] and Guido Toci[6]

[1]*Istituto di Fisica Applicata "Carrara", Consiglio Nazionale delle Ricerche, IFAC-CNR, via Madonna del Piano 10C, 50019 Sesto Fiorentino (FI), Italy*
[2]*Dipartimento di Chimica e Chimica Industriale, Università di Pisa, via Moruzzi 13, 56124 Pisa, Italy*
[3]*Ural Federal University named after the first President of Russia B.N. Yeltsin, Mira St. 19, Ekaterinburg 620002, Russian Federation*
[4]*Institute of Electrophysics UrB RAS, Amundsen St. 106, Ekaterinburg 620016, Russian Federation*
[5]*Dipartimento di Chimica "U. Schiff", Università di Firenze, Via della Lastruccia, 3-13, 50019 Sesto Fiorentino (FI), Italy*
[6]*Istituto Nazionale di Ottica, Consiglio Nazionale delle Ricerche, INO-CNR, via Madonna del Piano 10B, 50019 Sesto Fiorentino (FI), Italy*
[*]*a.pirri@ifac.cnr.it*

**Abstract:** We report on micro-Raman spectra of several mixed laser ceramics, i.e., 5*at.%*Tm:$(Sc_xY_{1-x}O_2)_3$ with x = 0.121, 0.252, 0.489 and 5*at.%*Tm:$Y_2O_3$ ceramic. The samples were fabricated by solid-state pressureless consolidation of nanopowders produced by laser ablation of solid target in air flow. In particular, we studied the influence of $Sc^{3+}$ content on the active vibration modes in terms of peak positions and shifts, linewidths and shapes: these parameters are relevant for the emission bandwidth of the laser medium. A shift towards higher frequencies is measured with the increase of the $Sc^{3+}$ content in all samples in particular in $(Tm_{0.048}Y_{0.463}Sc_{0.489}O_2)_3$ where the main Raman peaks are placed at 395, 494, 635 $cm^{-1}$ while their shifts with Tm:$Y_2O_3$ are 22.6, 25.1, 40.1 $cm^{-1}$, respectively. The assignment of the vibrational spectrum was obtained by density functional theory (DFT) with the Perdew-Burke-Enzerhof (PBE) exchange-correlation functional within the harmonic approximation framework.



## 1. Introduction

Among laser matrices with high thermal conductivities, $k_{th}$ (which is a fundamental property for developing laser system with high average power), both $Y_2O_3$ [1] and $Sc_2O_3$ [2] sesquioxides have attracted a great interest of the scientific community; low efficiency and power extraction as well as spatial distortion of the laser beam are usually addressed to low values of $k_{th}$ [3]. Single-crystals and transparent polycrystalline ceramics, hereon ceramics, doped with rare earth elements (RE) were manufactured by using different growth methods [4–7] and fabrication techniques [8–10] with excellent results in terms of high optical quality. Additionally, the relation between the preparation and quality of the powders and the sintering processes was clearly pointed out [11].

We focus on thulium trivalent ions ($Tm^{3+}$) as doping species because $Tm^{3+}$ is an excellent candidate for developing solid-state laser system with emission in the near and mid-infrared, i.e., from 1.9 to 2.3 µm [12–15]. Both $Tm^{3+}$-doped $Y_2O_3$ [16–19] and $Sc_2O_3$ [20–24] hosts were largely studied with excellent results. It is worth noting that the $Tm^{3+}$ $^3F_4 \rightarrow {}^3H_6$ emission at around 2 µm, commonly called "*eye-safe region*", plays an important role in many applications. This is because it is absorbed by human eye vitreous body so it cannot reach (and thus potentially

#518356 https://doi.org/10.1364/OE.518356
Journal © 2024 Received 15 Jan 2024; revised 1 Mar 2024; accepted 6 Mar 2024; published 17 Jun 2024

Optics EXPRESS

damage) the retina; moreover, it is not subjected to absorption by the water vapor in the atmosphere allowing free space propagation of CW and pulsed laser light, including ultrashort pulses.

Recently, RE-doped disordered sesquioxide matrices are being considered because preserve reasonable values of thermal conductivity and, at the same time, show a considerable inhomogeneous broadening of both emission and absorption cross sections useful for developing tunable and few-optical-cycle pulsed laser systems [25–27]. So far in $Tm^{3+}$-doped $(Y,Sc)_2O_3$ matrices [28] the role played by $Sc^{3+} \rightarrow Y^{3+}$ substitution on the $Tm^{3+}$ spectroscopic behavior was studied and its strong influence on the emission and absorption cross sections of $Tm^{3+}$ was clearly demonstrated [29,30]. This peculiar behavior of disordered ceramic matrices was confirmed by other studies, where $Yb^{3+}$ doped $(Y,Lu,Sc)_2O_3$ ceramics were investigated and the effects of $Sc^{3+}$ or $Lu^{3+}$ on the ytterbium spectroscopic features were carefully analyzed: it was found that ions with larger discrepancies in mass and radius heavily influence the spectroscopic characteristics of the active ions.

Last but not least, it is well known that both in garnets and in sesquioxides the absorption and emission spectra are determined not only by the Stark splitting of the energy levels of the dopant, but also by the occurrence of phonon-assisted transitions. Moreover, the excited level lifetimes and the cross-relaxation process in $Tm^{3+}$ are influenced by the phonon energy, as it is recalled for instance in [31]. Therefore, the increase in the Raman frequencies can, in principle, lead to the occurrence of more widely spaced phonon-assisted bands (contributing to the spectral broadening generated by the lattice disorder), along with stronger multi-phonon assisted non radiative processes. Both these effects influence the spectroscopic and lasing properties of the RE metal ions [31].

This paper is devoted to study the effect on $Sc^{3+}$/ $Y^{3+}$ ratio on the active vibration modes in several mixed laser ceramics, i.e., *5at.%*Tm:$(Sc_xY_{1-x}O_2)_3$ with x = 0, 0.121, 0.252, 0.489 by investigating their micro-Raman spectra. In particular, the role played by different radii and masses of $Y^{3+}$ and $Sc^{3+}$ on the position of the Raman peaks was investigated. The assignment of the vibration modes was obtained by using the Density Functional Theory (DFT) with the Perdew-Burke-Enzerhof (PBE) exchange-correlation functional within the harmonic approximation framework.

## 2. Materials and methods

### 2.1. Ceramic fabrication

In order to fabricate transparent $Tm^{3+}$-doped $(Sc_xY_{1-x})_2O_3$ ceramics, nanopowders with the corresponding chemical composition were used as the starting materials [32]. Nano-sized individual particles were synthesized by the laser ablation method. This involved evaporating a solid target material using $CO_2$-laser with the eventual condensation of the vapor carried out in air flow. The obtained nanopowders were annealed for 3 h at 1050 °C in air and then uniaxially pressed at 200 MPa into cylindrical-shaped green bodies having 14 mm diameter. The prepared compacts were calcined for 3 h at 800 °C in air.

Then, vacuum sintering (20 h at 1780 °C under a residual gas pressure of $10^{-3}$ Pa) was taking place. Next, the sintered ceramic samples were subjected to annealing for 2 h at 1400 °C for restoring oxygen stoichiometry and then mirror polished on both sides. The photographs of the used Tm:$(Y,Sc)_2O_3$ ceramics corresponding to $(Tm_{0.05}Y_{0.95})_2O$ or $Sc_0$, $(Tm_{0.05}Sc_{0.121}Y_{0.829})_2O_3$ or $Sc_{12}$, $(Tm_{0.05}Sc_{0.252}Y_{0.698})_2O_3$ or $Sc_{25}$ and $(Tm_{0.048}Y_{0.463}Sc_{0.489})_2O_3$ or $Sc_{50}$ are presented in Fig. 1. The thickness of all ceramics is 1.7 mm while the diameter ranges from 5 to 7 mm.

### 2.2. Micro-Raman investigation

The micro-Raman spectra of all ceramics were acquired by using a micro-Raman spectrometer RM2000 (Renishaw, Wotton-under-Edge, UK) equipped with a 50x/0.80 NA Olympus microscope

Optics EXPRESS

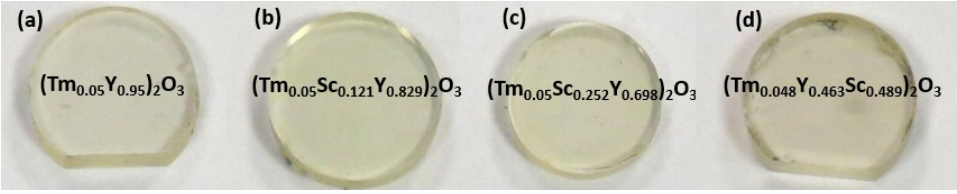


**Fig. 1.** Photographs of the ceramic samples: (a) $Sc_0$, (b) $Sc_{12}$, (c) $Sc_{25}$ and (d) $Sc_{50}$.

objective and an $Ar^+$ laser excitation-source with emission at 514.5 nm). The spectral calibration of the spectrometer was checked on the 520 $cm^{-1}$ first order Raman band of bulk silicon; the spectral resolution was 7 $cm^{-1}$ as verified from linewidth measurements on the same silicon calibration band. For each sample, twenty different micro-Raman spectra were acquired along a line with 20 µm spacing and at a depth of ~ 200 µm below the surface of the ceramic. The spatial resolution of the instrument was ~ 1 µm across and along the line of sight.

### 2.3. X-ray diffraction investigation

The XRD measurements were performed by using a D8 Discover diffractometer (Bruker AXS, Germany) equipped with an X-ray tube with a copper anode (CuKα1 λ = 1.5406 Å). The lattice parameters determined by the crystal structure refinement using the Rietveld method are 10.595 Å ($Sc_0$), 10.503 Å ($Sc_{12}$), 10.401 Å ($Sc_{25}$) and 10.216 Å ($Sc_{50}$), respectively.

### 2.4. Computational methods

The structural and the vibrational mode frequencies of all samples were calculated by the Density Functional Theory (DFT) performed with CP2 K software package [33] and using the Perdew-Burke-Enzerhof (PBE) exchange-correlation functional [34,35] with Grimme D3 dispersion correction [36] (obtained by taking into account the Van der Waals inter-atomic forces). The Goedecker-Teter-Hutter (GTH) pseudopotentials [37] with DZVP-MOLOPT-SR-GTH [38] basis set for the Y, Tm, Sc and O atoms were employed. Concerning the suitability of the selected basis set, it worth noting that it has a small basis set superposition error, and it is well conditioned, therefore, it is appropriate for a large variety of systems both in gas phase and in condensed phase. The calculation employed a cutoff energy of 1000 Ry and a normalized convergence threshold of $10^{-10}$ for the Self-Consistent Field (SCF) convergence and $10^{-5}$ hartree·$bohr^{-1}$ for the maximum force component. In particular, we start from an initial conventional unit cell geometry, obtained from the Material Project [39], which underwent structural optimization until stringent convergence criteria were satisfied. Specifically, the optimization parameters were set to ensure that the maximum displacement residue (which in the software corresponds to the output value MAX_DR) and maximum force residue (output value MAX_FORCE) remained below $1.0 \times 10^{-4}$ Bohr and $1.0 \times 10^{-5}$ $Bohr^{-1} \times$ Hartree, respectively. Additionally, the root mean square (output value RMS) criteria for displacement (output value RMS_DR) and force (output value RMS_FORCE) were constrained to be under $1.0 \times 10^{-4}$ Bohr and $1.0 \times 10^{-5}$ $Bohr^{-1} \times$ Hartree. Focusing on the procedure, as a first step we carried out a systematic optimization of the unit cell parameters and atomic coordinates using the Potential Energy Surface (PES) as merit function. This allowed uncovering metastable configurations situated at local minima of the Potential Energy Surface (PES). The conventional unit cell representative of a Tm:$(Sc,Y)_2O_3$ ceramic, comprising 80 constituent atoms (16 cell formula units, Z = 16), is depicted in Fig. 2.

Optics EXPRESS

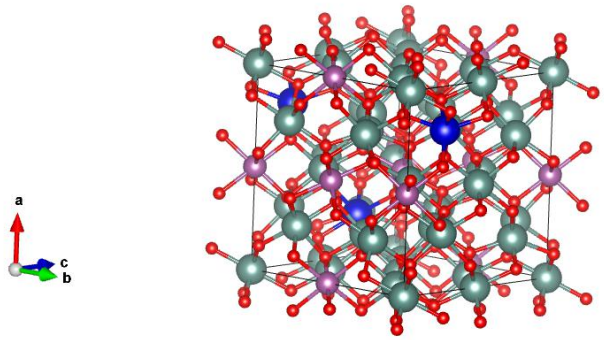


**Fig. 2.** Unit cell of the Tm:$(Sc,Y)_2O_3$: O (red balls), Sc (violet balls), Y (grey balls), Tm (blue balls). Graphical representation generated by using Vesta software [40].

## 3. Experimental and computational results

In Fig. 3(a) we report the micro-Raman spectra of all ceramics recorded at room temperature. Each spectrum shows one intense band ($R_1$) and two weaker bands with a comparable intensity ($R_2$ and $R_3$), which is very common for a c-type $RE_2O_3$ (RE = Y, Lu, Sc) hosts [41].

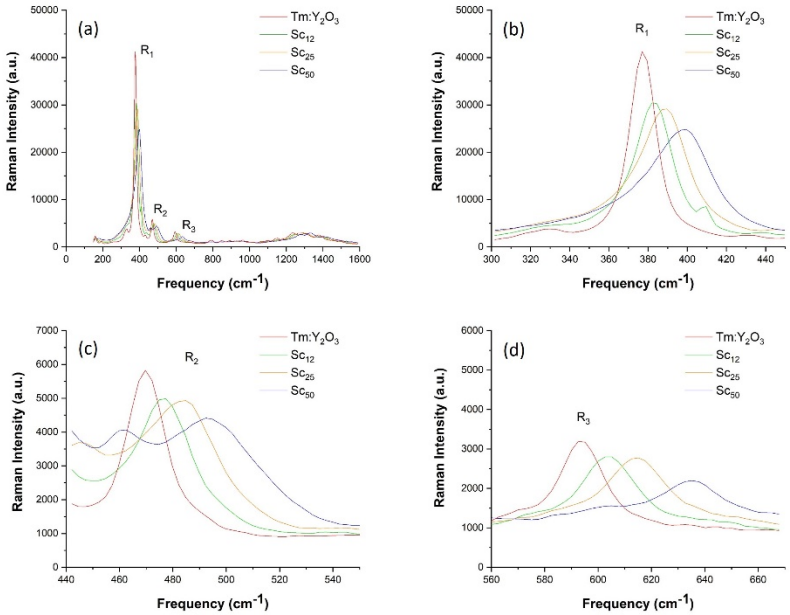


**Fig. 3.** Micro Raman spectra of all ceramics (a) acquired at room temperature. $R_1$, $R_2$, $R_3$ label on the graph the main Raman modes. In (b), (c) and (d) panels an expanded view of the relevant spectral ranges is shown.

We have taken as a reference the $(Tm_{0.05}Y_{0.95})_2O_3$ sample to elucidate the effect of the Sc→Y substitution. Its Raman spectrum shows three main peaks at 377 ($R_1$), 460 ($R_2$) and 595 ($R_3$) $cm^{-1}$ with a corresponding linewidth of 16.4, 15.3, and 18.6 $cm^{-1}$, respectively, in good agreement with literature [41,42]. Also, a rather weak, broad band at 1200-1400 $cm^{-1}$ was observed but, as cannot be ascribed to fundamental Raman active modes, we are not able to provide an assignment for it. The increase of the $Sc^{3+}/Y^{3+}$ ratio (from $Sc_0$ to $Sc_{50}$) influences

Optics EXPRESS

the main peaks wavenumber in the mixed ceramics. The peaks are *quasi*-linearly shifted toward higher wavenumbers with increased $Sc^{3+}$ content, see Fig. 3(b)-(d). Among the different Raman bands, $R_3$ is the most influenced by the concentration of scandium as a shift up to 40.12 $cm^{-1}$ was observed, see Fig. 2(d). Concerning the linewidth, all active modes showed a broadening that increases with the Sc concentration: $R_1$ linewidth, for instance, ranges from 16.39 in $Sc_0$ to 38.88 $cm^{-1}$ in $Sc_{50}$. In Fig. 4 is shown the shift of the main Raman bands versus the $Sc^{3+}$ content, while Table 1 reports the values of both the wavenumber of the Raman peaks and the corresponding shifts. The wavenumber of the peaks as well as the corresponding linewidths were determined by a Gaussian fit of the bands. From this analysis it was extrapolated the standard deviation, $\sigma_{sd}$, in the determination of the $R_3$ peak wavenumber and we used it to estimate an upper limit of the fluctuation of the $Sc^{3+}/Y^{3+}$ ratio in the probe volume taking into account the dependence of the Raman mode shift on the $Sc^{3+}$ content as reported in Fig. 3. The $R_3$ band was selected for performing the analysis because it shows the highest shift value among the active Raman-modes and therefore it represents the most sensitive probe. We note that the underpinning assumption, i.e., the shift is due to the increase of $Sc^{3+}$ ion concentration, is correct because of additional error sources can be considered within the measurement accuracy. Along the transect the calculated $\sigma_{sd}$ for the $R_3$ active mode wavenumber was 0.30 $cm^{-1}$ corresponding to an indetermination of 0.40 *at.%* in the $Sc^{3+}$ content.

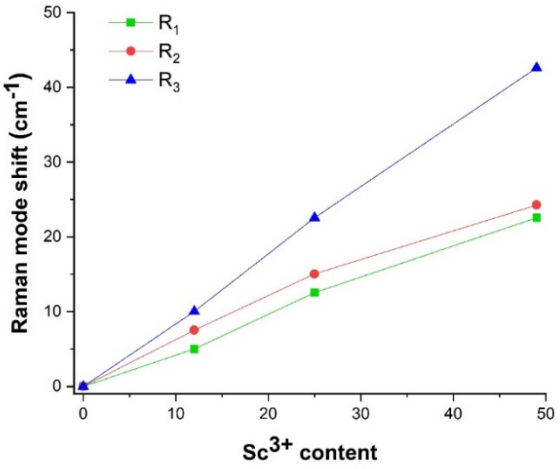


**Fig. 4.** Raman mode shift of the three main peaks as a function of the $Sc^{3+}$ content.

**Table 1. Peaks position of $R_j$ and corresponding Raman shift S(Rj), j = 1,2,3**

| | Peak position ($cm^{-1}$) | | | Shift ($cm^{-1}$) | | |
|---|---|---|---|---|---|---|
| Material | $R_1$ | $R_2$ | $R_3$ | $S(R_1)$ | $S(R_2)$ | $S(R_3)$ |
| $Sc_0$ | 377,31 | 469,73 | 595,1 | 0 | 0 | 0 |
| $Sc_{12}$ | 382,41 | 477,26 | 605,13 | 7,52 | 7,53 | 10,03 |
| $Sc_{25}$ | 387,17 | 484,78 | 615,16 | 12,54 | 15,05 | 20,06 |
| $Sc_{50}$ | 395,11 | 494,81 | 635,22 | 22,57 | 25,08 | 40,12 |

It is important to remark that micro-Raman mapping data can be used to assess uniformity in the distribution of yttrium and scandium ions inside the ceramics. Their spatial distribution results homogeneous as from the comparison between the 20 spectra acquired for each sample taken at a distance of 20 µm each along a line, we do not observe changes in the shape, linewidth

Optics EXPRESS

and position for the different bands along the scan. Moreover, as additional peaks are not observed along the spectra, it can be excluded the presence of $Y_2O_3$ and $Sc_2O_3$ phases in agreement with the XRD data (see Fig. 5). As an example, in Fig. 6 the Raman spectra measured along a 400 µm line on the $Sc_{12}$ sample are shown.

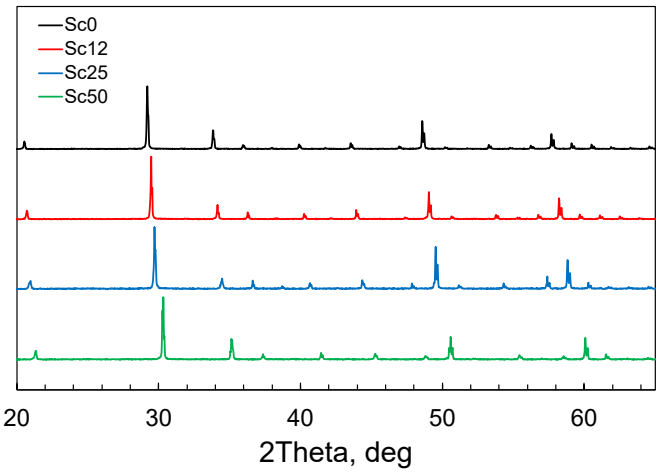


**Fig. 5.** XRD patterns of the fabricated ceramic samples.

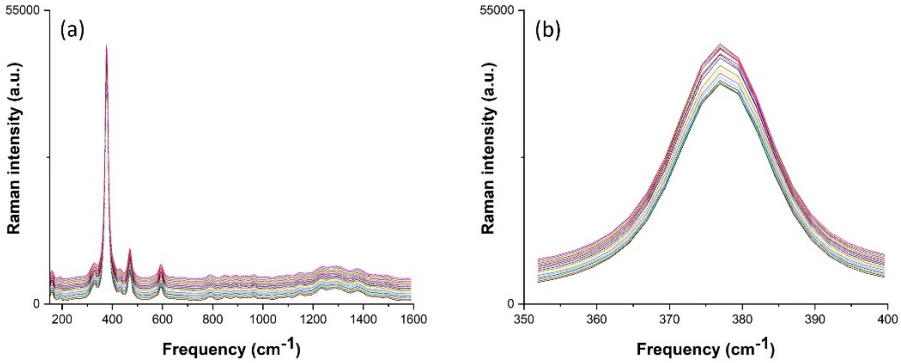


**Fig. 6.** Raman spectra of the $Sc_{12}$ ceramic acquired in 20 different points equally spaced along a 400 µm line at step of 20 µm (a) and the zoom of the most intense mode (b). For the sake of clarity, the spectra have been shifted along the y-axis.

Within pure Yttrium Oxide ($Y_2O_3$) ceramics, the determination of cubic unit cell symmetry results in assigning the $Ia\bar{3}$ space group. While the variation of ionic radius between $Y^{3+}$ and $Sc^{3+}$ degrades the lattice symmetry in Tm:$(Sc,Y)_2O_3$ ceramics, owing to the local distortions, the $Ia\bar{3}$ classification was still used (although approximately) to keep trace of the relationship of the Raman modes of the distorted lattice with the parent one.

Later on, the analysis of the normal modes of vibration of the system was carried out by using the DFT, within the harmonic approximation framework and the Born-Oppenheimer approximation. Briefly, by applying the Hellmann-Feynman theorem, the forces acting on each atom were deduced from the derivatives of the total energy with respect to the atomic positions. The derivation of the Hessian matrix ensued, which involved computing the second derivatives of the total energy relative to atomic displacements. The resultant Hessian matrix describes

Optics EXPRESS

the curvature of the potential energy surface around equilibrium geometries. By the Hessian matrix diagonalization, the vibrational frequencies (i.e., eigenvalues) were extracted, while the corresponding eigenvectors defined the distinct vibrational modes.

Starting from $Y_2O_3$ host, the frequencies of the vibrational modes at Γ point were calculated by PBE and to each vibrational mode was assigned the irreducible representations belonging to the space group $Ia\bar{3}$ as reported in the following equation:

$$\Gamma = 4\boldsymbol{A_g} + 4\boldsymbol{E_g} + 14\boldsymbol{F_g} + 5\boldsymbol{A_{2u}} + 5\boldsymbol{E_u} + 16\boldsymbol{F_u} \quad (1)$$

where $4\boldsymbol{A_g} + 4\boldsymbol{E_g} + 14\boldsymbol{F_g}$ are Raman active modes, $16\boldsymbol{F_u}$ are infrared active modes and $5\boldsymbol{A_{2u}}$, $5\boldsymbol{E_u}$ are inactive modes.

In Table 2 are reported the experimental and calculated data for undoped $Y_2O_3$ host; as it can be pointed out from Δ% values there is a good agreement between the experimental [43] and calculated data which validates our theoretical approach.

**Table 2. Experimental [43] and calculated frequencies for the vibrational modes of $Y_2O_3$ matrix. The percentage relative deviation Δ% is also provided in support of the proposed assignment. n.a. stands for "not available" in [43].**

| Sym | exp | PBE | Δ% | Sym | exp | PBE | Δ% |
|---|---|---|---|---|---|---|---|
| | 591 | 604.6 | 2.15% | | 564 | 556.2 | 1.36% |
| $\mathbf{A_g}$ | 469 | 465.3 | 0.79% | $\mathbf{E_g}$ | 429 | 428 | 0.23% |
| | 376 | 378.5 | 0.66% | | 329 | 326 | 0.91% |
| | 161 | 163.6 | 1.61% | | 193 | 190.7 | 1.91% |
| | 591 | 589.8 | 0.21% | | 575 | 580.2 | 0.89% |
| | 564 | 569.7 | 1.01% | | 555 | 556.2 | 0.22% |
| | 526 | 534.3 | 1.63% | | 490 | 506.5 | 3.37% |
| | 469 | 473.1 | 0.87% | | 462 | 456.8 | 1.13% |
| | 429 | 436.5 | 1.75% | | 430 | 445 | 3.49% |
| | 399 | 400.2 | 0.30% | | 415 | 414.9 | 0.02% |
| | 376 | 382 | 1.59% | | 372 | 370.4 | 0.43% |
| $\mathbf{F_g}$ | 329 | 333.7 | 1.43% | $\mathbf{F_u}$ | 335 | 338.2 | 0.96% |
| | 318 | 317.6 | 0.12% | | 302 | 304.3 | 0.76% |
| | 193 | 194.6 | 0.83% | | 242 | 237.4 | 1.90% |
| | 179 | 176.7 | 1.28% | | 183 | 182.1 | 0.49% |
| | 161 | 168.5 | 4.45% | | 172 | 173.3 | 0.76% |
| | 129 | 123.4 | 4.30% | | n.a. | 167.5 | - |
| | 116 | 114.1 | 1.64% | | n.a. | 150.3 | - |
| | | | | | 120 | 119.6 | 0.33% |
| | | | | | n.a. | 108 | - |

Vibrational modes simulations performed by using the compositions of our samples, i.e., 5.0 *at.%* Tm-doped $Y_2O_3$, $Sc_{12}$, $Sc_{25}$, and $Sc_{50}$, allowed us to assign the irreducible representation to each vibrational mode as depicted in Fig. 7. In particular, $R_1$, $R_2$ and $R_3$, which labelled the most intense Raman active modes in Fig. 3, correspond to $A_g + F_g$ irreducible representations. Table 3 reports the experimental and calculated Raman frequencies at different concentrations of $Sc^{3+}$ and percentage relative deviation Δ%. Also in this case, a good agreement between the experimental and calculated values is found.

The vibrational active modes within the ranges of 590-640 $cm^{-1}$, 430-500 $cm^{-1}$, and 376-402 $cm^{-1}$ are due to metal-oxygen stretching and metal-oxygen-metal or oxygen-metal-oxygen

Optics EXPRESS

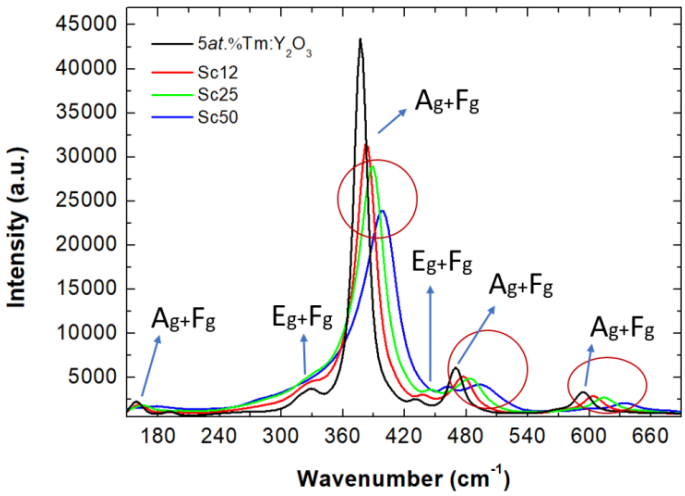


**Fig. 7.** Experimental spectra and Raman active modes assignment. $Rj = A_g + F_g$ with $j = 1,2,3$.

**Table 3. Frequencies at different concentrations of $Sc^{3+}$ and percentage relative deviation Δ%**

| Sym | conc. | our exp. | PBE | Δ% |
|---|---|---|---|---|
| $\mathbf{A_g + F_g\ (R_1)}$ | $\mathbf{Sc_0}$ | 376.96 | 380.25 | 0.87% |
| | $\mathbf{Sc_{12}}$ | 381.98 | 387.79 | 1.52% |
| | $\mathbf{Sc_{25}}$ | 389.5 | 393.03 | 0.91% |
| | $\mathbf{Sc_{50}}$ | 399.53 | 403.36 | 0.96% |
| $\mathbf{A_g + F_g\ (R_2)}$ | $\mathbf{Sc_0}$ | 469.73 | 469.2 | 0.11% |
| | $\mathbf{Sc_{12}}$ | 477.26 | 473.79 | 0.73% |
| | $\mathbf{Sc_{25}}$ | 482.27 | 480.66 | 0.33% |
| | $\mathbf{Sc_{50}}$ | 494.2 | 499.03 | 0.99% |
| $\mathbf{A_g + F_g\ (R_3)}$ | $\mathbf{Sc_0}$ | 592.59 | 596.45 | 0.65% |
| | $\mathbf{Sc_{12}}$ | 602.62 | 602.61 | 0.00% |
| | $\mathbf{Sc_{25}}$ | 615.16 | 612.13 | 0.49% |
| | $\mathbf{Sc_{50}}$ | 632.71 | 631.58 | 0.18% |

bending modes. However, the contribution to each mode given by stretching and bending motions are different. Within the 590-640 $cm^{-1}$ range, the active modes are mainly addressed to stretching motion. Conversely, the vibration modes within the 376-402 $cm^{-1}$ and 430-500 $cm^{-1}$ bands are due to both stretching and bending motions.

Finally, we calculated the elastic constants using the CASTEP software packages [44] performing calculations at DFT level with PBEsol functional. Once the elements of the $6 \times 6$ matrix of elastic constants were obtained, the Young's modulus and the Debye's temperature were calculated [45,46].

Our structural calculations, see Table 4, clearly demonstrate that by increasing the $Sc^{3+}$ concentration a volume contraction of the unit cell (as shown by the cell unit parameter $a_{PBE}$) and an enhancement of the rigidity of the disordered ceramics (resulting in increasing Debye's temperatures, $\theta_D$ and Young's modulus, E) occur. The knowledge of the $\theta_D$ and E parameters assumes a particular significance because it is linked to the average energy of atomic lattice vibrations and quantifies the material resistance to deformations, therefore, it gives valuable

Optics EXPRESS

information on both the material rigidity and the average bond lengths present in the crystalline structure. High $\theta_D$ and E indicate stronger interatomic bonds and a higher rigidity of the structure. It worth noting the excellent agreement between experimental lattice parameters, $a_{exp}$, acquired by XRD measurements, and the calculated values $a_{PBE}$.

**Table 4. Structural parameters of the ceramics**

| Materials | $a_{exp}$ (Å) | $a_{PBE}$ (Å) | $\theta_D$ (K) | E (GPa) |
|---|---|---|---|---|
| Tm:$Y_2O_3$ | 10.595 | 10.599 | 470 | 167.3 |
| $Sc_{12}$ | 10.503 | 10.516 | 483 | 169.2 |
| $Sc_{25}$ | 10.401 | 10.418 | 497 | 171.5 |
| $Sc_{50}$ | 10.216 | 10.234 | 535 | 181.3 |

## 4. Discussion

We can summarize our results as follows. First, all Raman spectra are characterized by three main bands with a different intensity. Second, the substitution of some $Y^{3+}$ ions by $Sc^{3+}$ in the $Y_2O_3$ matrix influence the Raman spectra of the samples. Third, the effects of this substitution on the Raman peaks increase by increasing the $Sc^{3+}$ concentration and the effect is not uniform for the different bands and could be related to the nature of the vibration involved (stretching, bending or a combination of these motions). Starting from the intensity of the main bands, all micro-Raman spectra are characterized by bands with different peak intensities. This behavior is explained considering the variation of the polarizability during the vibrations: more intense peaks are related to higher values of polarizability. Accordingly, only 3 active modes can be observed along the scans, although many active modes are expected from 200 to 800 $cm^{-1}$. Theoretically, it can be observed the partial removal of degeneracy of the highly symmetric modes (i.e., $A_g/F_g$ and $E_g/F_g$) and the partial overlapping of the modes with different symmetries called $A_g + F_g$ and $E_g + F_g$ with the increase in Sc concentration. The shift toward higher Raman frequency increasing the $Sc^{3+}$ concentration, as clearly shown in Fig. 1(b)-(d), can be addressed to the different values of the mass and radius of the $Sc^{3+}$ and $Y^{3+}$. It can be theoretically explained within the harmonic approximation framework as the Raman mode frequency, $\omega$, is linked to the elastic constant $k$ and the reduced mass of the RE-O system, $m_r$, by the following formula:

$$\omega^2 = \frac{k}{m_r} \tag{2}$$

The wavenumber of the Raman peaks results from the interplay between $k$ and $m_r$. The decrease of the mass from 88.9 amu ($Y^{3+}$) to 44.95 amu ($Sc^{3+}$) drives the Raman peaks towards higher wavenumber values. Simultaneously, the discrepancy in ionic radii between $Sc^{3+}$ and $Y^{3+}$ (respectively 0.75 Å and 0.90 Å in VI-fold coordination by oxygen) induces localized lattice distortions. The increasing presence of the smaller $Sc^{3+}$ ion reduces the unit cell parameter and the bond lengths by decreasing the RE-O distances, consequently k increases (see Figs. 8 and 9). The combined effect of reduced mass and lattice distortions, influenced by ionic radii disparities, push the measured shifts of the Raman peaks towards higher values. From the analysis of our data, we do not observe a splitting of the different Raman bands because of the atomic substitution. A simple evaluation of the shift in the vibrational bands with isotopic substitution, carried out taking into account simply the different masses involved in the RE-O stretching (RE = Y or Sc) leads to a frequency change in the order of 5%. If the vibrations could be treated as local vibrational modes, a band splitting should be experimentally observable. Instead, we observe single (even if broad) bands suggesting the validity of a non-local approach. The vibrational analysis was performed using the CP2 K software. The calculated k and $m_r$ values are reported in Table 5.

Optics EXPRESS

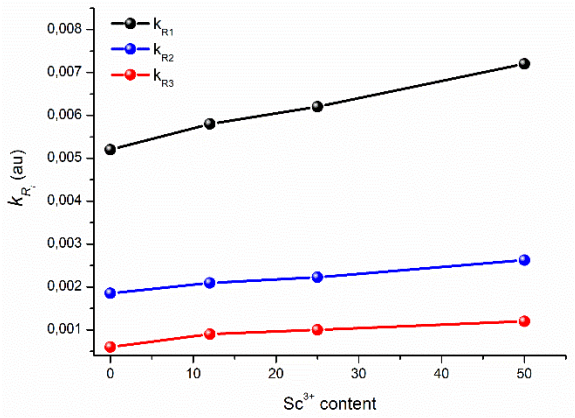


**Fig. 8.** Trend of the elastic constant $k_{R1}$, $k_{R2}$ and $k_{R3}$ versus the $Sc^{3+}$ content.

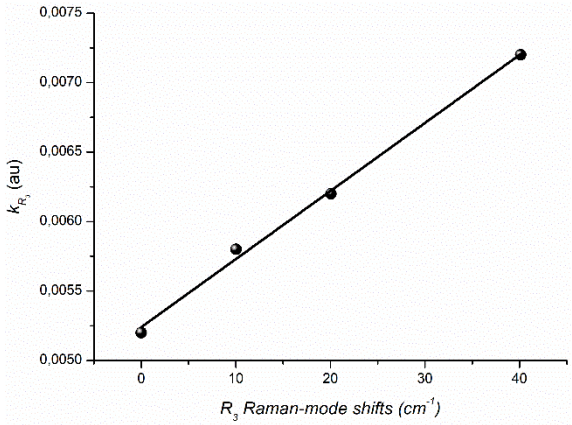


**Fig. 9.** Trend of the elastic constants $k_{R3}$ versus the $R_3$ Raman-mode shifts. The solid line represents the best linear-fit.

**Table 5. Calculated reduced masses $m_{rRj}$ and force constants $k_{Rj}$ associated to $R_j$ (j = 1,2,3) in atomic units (au)**

| Materials | $m_{rR1}$ (au) | $k_{R1}$ (au) | $m_{rR2}$ (au) | $k_{R2}$(au) | $m_{rR3}$ (au) | $k_{R3}$(au) |
|---|---|---|---|---|---|---|
| Tm:$Y_2O_3$ | 16.6143 | 0.0006 | 16.1372 | 0.0019 | 16.6284 | 0.0052 |
| $Sc_{12}$ | 16.8431 | 0.0009 | 16.2246 | 0.0021 | 17.1895 | 0.0058 |
| $Sc_{25}$ | 17.0456 | 0.0010 | 16.2699 | 0.0022 | 17.2709 | 0.0062 |
| $Sc_{50}$ | 17.5908 | 0.0012 | 16.5265 | 0.0026 | 17.6242 | 0.0072 |

Optics EXPRESS

Figure 10 shows the lattice parameters as a function of the Raman-mode shifts. The shift experienced by $R_1$, $R_2$ and $R_3$ depends on $Sc^{3+}$ content and increases from $Sc_0$ to $Sc_{50}$. However, $R_3$ band is subjected to higher values of shift values in all the samples. To explain it one should considered the sources of the Raman modes, which, as already mentioned in the previous paragraph, are due to different vibration motions, see Fig. 7. $R_3$ is assigned as a pure stretching motion while $R_1$ and $R_2$ are combinations of both stretching and bending motions. As the substitution of $Y^{3+}$ by $Sc^{3+}$ ions change the bond lengths of the RE-O system, the frequencies of the Raman modes characterized by a greater contribute of stretching motions are more shifted by the increase of the $Sc^{3+}$ concentration. This trend was already outlined in phonon dynamics studies on isotopically substituted molecular crystals [47].

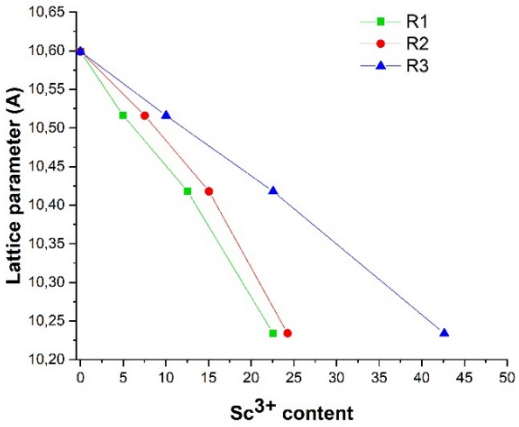


**Fig. 10.** Experimental lattice parameters versus Raman-mode shifts of the R1, R2 and R3 bands.

Last, the broadening of the linewidth of the Raman peaks from $Sc_0$ to $Sc_{50}$, see Fig. 3(c)-(d) can be considered an effect due to the growing increase of the disorder introduced in $Y_2O_3$ host; the higher the level of disorder in substitutional solid solutions $(Y,Sc)_2O_3$, the broader the Raman peaks.

Finally, concerning the role played by $Tm^{3+}$ on the active Raman modes, the effect of active ion is negligible as reported in Table 6, where the position peaks of the 5at.%Yb:$Y_2O_3$ and $Y_2O_3$ are compared [43].

**Table 6. Peaks position of $R_j$ with j = 1,2,3 measured in 5*at*%$Y_2O_3$ and $Y_2O_3$**

| | Peak position ($cm^{-1}$) | | |
|---|---|---|---|
| Material | $R_1$ | $R_2$ | $R_3$ |
| $Sc_0$ | 377.3 | 469.7 | 595.1 |
| $Y_2O_3$ | 376.0 | 469.0 | 591.0 |

## 5. Conclusions

We have presented the Raman investigation of the several 5*at.*%Tm-doped $(Sc_xY_{1-x}O_2)_3$ with x = 0, 0.121, 0.252, 0.489 mixed ceramics, which were fabricated by solid-state pressureless consolidation of nanopowders produced by laser ablation of solid target in air flow. The results were interpreted by using the Density Functional Theory (DFT) with the Perdew-Burke-Enzerhof (PBE) exchange-correlation functional within the harmonic approximation framework. Three

Optics EXPRESS

main bands were observed in all Raman spectra where the corresponding peak positions are strictly related to the $Sc^{3+}/Y^{3+}$ ratio. Additionally, it is worth noting that higher shift values are associated to stretching vibration motions rather than bending motions. As a matter of fact, we have measured the largest shift of the $R_3$ Raman peak within the 592-632 $cm^{-1}$ range. Also, the (almost) linear dependency of Raman shifts, lattice parameters and elastic constants to the $Sc^{3+}$ ion concentration in the ceramic was clearly demonstrated.

**Funding.** Russian Foundation for Basic Research (18-53-7815 Ital_t); Consiglio Nazionale delle Ricerche (SAC.AD002.020.016).

**Acknowledgments.** We wish to thank Mr. Mauro Pucci at INO-CNR for the laser-grade optical polishing of the samples used in the experiments.

**Disclosures.** The authors declare no conflicts of interest.

**Data availability.** Data underlying the results presented in this paper are not publicly available at this time but may be obtained from the authors upon reasonable request.

## References

1. K. Petermann, L. Fornasiero, E. Mix, *et al.*, "High melting sesquioxides: Crystal growth, spectroscopy, and laser experiments," Opt. Mater. **19**(1), 67–71 (2002).
2. B. L. Garrec, V. Cardinali, and G. Bourdet, "Thermo-optical measurements of ytterbium doped ceramics ($Sc_2O_3$, $Y_2O_3$, $Lu_2O_3$, YAG) and crystals (YAG, $CaF_2$) at cryogenic temperatures," Proc. SPIE **8780**, 87800E (2013).
3. R. Gaumè, B. Viana, D. Vivien, *et al.*, "A simple model for the prediction of thermal conductivity in pure and doped insulating crystals," Appl. Phys. Lett. **83**(7), 1355–1357 (2003).
4. S. S. Ballard, K. A. McCarthy, and C. D. William, "A method for measuring the thermal conductivity of small samples of poorly conducting materials such as optical crystals," Rev. Sci. Instrum. **21**(11), 905–907 (1950).
5. V. Peters, A. Bolz, K. Petermann, *et al.*, "Growth of high-melting sesquioxides by the heat exchanger method," J. Cryst. Growth **237-239**, 879–883 (2002).
6. A. Fukabori, V. Chani, K. Kamada, *et al.*, "Growth of $Tm^{3+}$-doped $Y_2O_3$, $Sc_2O_3$, and $Lu_2O_3$ crystals by the micropulling down technique and their optical and scintillation characteristics," Cryst. Growth Des. **11**(6), 2404–2411 (2011).
7. M. Guzik, J. Pejchal, A. Yoshikawa, *et al.*, "Structural investigations of $Lu_2O_3$ as single crystal and polycrystalline transparent ceramic," Cryst. Growth Des. **14**(7), 3327–3334 (2014).
8. X. Lu, B. Jiang, J. Li, *et al.*, "Synthesis of highly sinterable Yb:$Sc_2O_3$ nanopowders for transparent ceramic," Ceram. Int. **39**(4), 4695–4700 (2013).
9. M. G. Chapman, R. C. Walker II, J. M. Schmitt, *et al.*, "Effects of sintering temperature on open-volume defects and thermoluminescence of Yttria and Lutetia ceramics," J. Am. Ceram. Soc. **99**(4), 1449–1454 (2016).
10. S.-Z. Lu and Q.-H. Yang, "Spectroscopic characterization of Yb:$Sc_2O_3$ transparent ceramics," Chin. Phys. B **21**(4), 047801 (2012).
11. A. C. Bravo, L. Longuet, D. Autissier, *et al.*, "Influence of the powder preparation on the sintering of Yb-doped $ScY_2O_3$ transparent ceramics," Opt. Mater. **31**(5), 734–739 (2009).
12. B. M. Walsh, "Review of Tm and Ho materials; spectroscopy and lasers," Laser Phys. **19**(4), 855–866 (2009).
13. T. Becker, R. Clausen, G. Huber, *et al.*, "Spectroscopic and Laser Properties of Tm-Doped YAG at 2 µm," in *Advanced Solid State Lasers*, M. Shand and H. Jenssen, eds., Vol. 5 of OSA Proceedings Series (Optical Society of America, 1989), paper DD1.
14. J. A. Caird, L. G. DeShazer, and J. Nella, "Characteristics of room-temperature 2.3-µm laser emission from $Tm^{3+}$ in YAG and $YALO_3$," IEEE J. Quantum Electron. **11**(11), 874–881 (1975).
15. A. Pirri, R. N. Maksimov, J. Li, *et al.*, "Achievements and future perspectives of the trivalent thulium-ion-doped mixed-sesquioxide ceramics for laser applications," Materials **15**(6), 2084 (2022).
16. F. Yue, V. Jambunathan, S. P. David, *et al.*, "Spectroscopy and diode-pumped continuous-wave laser operation of Tm:$Y_2O_3$ transparent ceramic at cryogenic temperatures," Appl. Phys. B **126**(3), 44 (2020).
17. F. S. Ermeneux, Y. Sun, R. L. Cone, *et al.*, "Efficient CW 2 µm Tm3+:Y2O3 Laser," in *Advanced Solid State Lasers*, M. Fejer, H. Injeyan, and U. Keller, eds., Vol. 26 of OSA Trends in Optics and Photonics (Optical Society of America, 1999), paper TuB8.
18. J. W. Szela, K. A. Sloyan, T. L. Parsonage, *et al.*, "Laser operation of a Tm:$Y_2O_3$ planar waveguide," Opt. Express **21**(10), 12460–12468 (2013).
19. H. Wang, H. Huang, P. Liu, *et al.*, "Diode-pumped continuous-wave and Q-switched Tm:$Y_2O_3$ ceramics laser around 2050nm," Opt. Mater. Express **7**(2), 296–303 (2017).
20. P. Koopmann, S. Lamrini, K. Scholle, *et al.*, "Long wavelength laser operation of Tm:$Sc_2O_3$ at 2116 nm and beyond," in *Advanced Solid-State Photonics* (2011), paper ATuA5.
21. A. A. Lagatsky, P. Koopmann, P. Fuhrberg, *et al.*, "Passively mode locked femtosecond Tm:$Sc_2O_3$ laser at 2.1 µm," Opt. Lett. **37**(3), 437–439 (2012).

Optics EXPRESS


22. A. Suzuki, C. Krankel, and M. Tokurakawa, "High quality-factor Kerr-lens mode-locked Tm:$Sc_2O_3$ single crystal laser with anomalous spectral broadening," Appl. Phys. Express **13**(5), 052007 (2020).
23. M. Tokurakawa, E. Fujita, A. Suzuki, *et al.*, "Sub-120 fs Kerr-lens mode-locked Tm:$Sc_2O_3$ laser at 2.1 μm wavelength range," *International Conference Laser Optics* (2018).
24. V. Lupei, A. Lupei, C. Gheorghe, *et al.*, "Spectroscopic characteristics of $Tm^{3+}$ in Tm and Tm, Nd, Yb:$Sc_2O_3$ ceramic," J. Lumin. **128**(5-6), 901–904 (2008).
25. Y. Wang, Y. Zhao, Z. Pan, *et al.*, "78 fs SWCNT-SA mode-locked Tm:CLNGG disordered garnet crystal laser at 2017nm," Opt. Lett. **43**(17), 4268–4271 (2018).
26. L. Wang, W. Chen, Y. Zhao, *et al.*, "Sub-50 fs pulse generation from a SESAM mode-locked Tm,Ho-codoped calcium aluminate laser," Opt. Lett. **46**(11), 2642–2645 (2021).
27. L. Wang, W. Chen, Z. Pan, *et al.*, "Sub-100 fs mode-locked Tm:CLTGG laser," Opt. Express **29**(20), 31137–31144 (2021).
28. Y. Feng, G. Toci, B. Patrizi, *et al.*, "Fabricaion, microstructure, and optical properties of Tm:$Y_3ScAl_4O_{12}$ laser ceramics," J. Am. Ceram. Soc. **103**(3), 1819–1830 (2020).
29. A. Pirri, R. N. Maksimov, V. A. Shitov, *et al.*, "Continuously tuned $(Tm_{0.05}Sc_{0.2522}Y_{0.698})_2O_3$ ceramic laser with emission peak at 2076nm," J. Alloys Compd. **889**, 161585 (2021).
30. A. Pirri, B. Patrizi, R. N. Maksimov, *et al.*, "Spectroscopic investigation and laser behaviour of Yb-doped laser ceramics based on mixed crystalline structure $(Sc_xY_{1-x})_2O_3$," Ceram. Int. **47**(20), 29483–29489 (2021).
31. K. Eremeev, P. Loiko, S. Balabanov, *et al.*, "Spectroscopy of thulium ions in solid-solution sesquioxide laser ceramics: Inhomogeneous spectral line broadening, crystal-field engineering and $C_{3i}$ sites," Opt. Mater. **148**, 114791 (2024).
32. V. V. Osipov, V. V. Platonov, V. V. Lisenkov, *et al.*, "Production of nanopowders of oxides by means of fiber and pulse-periodical $CO_2$ lasers," Phys. Status Solidi C **10**(6), 926–932 (2013).
33. T. D. Kühne, M. Iannuzzi, M. Del Ben, *et al.*, "CP2K: An Electronic Structure and Molecular Dynamics Software Package - Quickstep: Efficient and Accurate Electronic Structure Calculations," J. Chem. Phys. **152**(19), 194103 (2020).
34. J. P. Perdew, "Climbing the Ladder of Density Functional Approximations," MRS Bull. **38**(9), 743–750 (2013).
35. J. P. Perdew, M. Ernzerhof, and K. Burke, "Rationale for Mixing Exact Exchange with Density Functional Approximations," J. Chem. Phys. **105**(22), 9982–9985 (1996).
36. S. Grimme, J. Antony, S. Ehrlich, *et al.*, "A Consistent and Accurate Ab Initio Parametrization of Density Functional Dispersion Correction (DFT-D) for the 94 Elements H-Pu," J. Chem. Phys. **132**(15), 154104 (2010).
37. S. Goedecker, M. Teter, and J. Hutter, "Separable Dual-Space Gaussian Pseudopotentials," Phys. Rev. B **54**(3), 1703–1710 (1996).
38. J. VandeVondele and J. Hutter, "Gaussian Basis Sets for Accurate Calculations on Molecular Systems in Gas and Condensed Phases," J. Chem. Phys. **127**(11), 114105 (2007).
39. M. de Jong, W. Chen, T. Angsten, *et al.*, "Charting the complete elastic properties of inorganic crystalline compounds," Sci. Data **2**(1), 150009 (2015).
40. K. Momma and F. Izumi, "VESTA: A Three-Dimensional Visualization System for Electronic and Structural Analysis," J. Appl. Crystallogr. **41**(3), 653–658 (2008).
41. N. D. Todorov, M. V. Abrashev, V. Marinova, *et al.*, "Raman spectroscopy and lattice dynamical calculations of $Sc_2O_3$ single crystals," Phys. Rev. B **87**(10), 104301 (2013).
42. A. Ubaldini and M. M. Carnasciali, "Raman characterization of powder of cubic $RE_2O_3$ (RE = Nd, Gd, Dy, Tm, and Lu), $Sc_2O_3$ and $Y_2O_3$," J. Alloys Compd. **454**(1-2), 374–378 (2008).
43. Y. Repelin, C. Proust, E. Husson, *et al.*, "Vibrational Spectroscopy of the C-Form of Yttrium Sesquioxide," J. Solid State Chem. **118**(1), 163–169 (1995).
44. S. J. Clark, M. D. Segall, C. J. Pickard, *et al.*, "First Principles Methods Using CASTEP," Z. Kristallogr. - Cryst. Mater. **220**(5-6), 567–570 (2005).
45. X. Zhang, W. Gui, and Q. Zeng, "First-Principles Study of Structural, Mechanical, and Thermodynamic Properties of Cubic $Y_2O_3$ under High Pressure," Ceram. Int. **43**(3), 3346–3355 (2017).
46. X. Zhang, S. Gao, W. Gui, *et al.*, "First-Principles Study of Structure, Mechanical and Optical Properties of La-and Sc-Doped $Y_2O_3$," J. Rare Earths **37**(8), 879–885 (2019).
47. J. P. Pinan, R. Ouillon, P. Ranson, *et al.*, "High resolution Raman study of phonon and vibron bandwidths in isotopically pure and natural benzene crystal," J. Chem. Phys. **109**(13), 5469–5480 (1998).